The Astrophysical Journal, 1004:137 (11pp), 2026 June 20 https://doi.org/10.3847/1538-4357/ae657e

WFST Supernovae in the First Year. III. Systematical Study of the Photometric Behavior of Early-phase Core-collapse Supernovae

Junhan Zhao[1,2], Ji-an Jiang[1,3], Zelin Xu[1,2], Yu-Hao Zhang[4,5,6], Qiliang Fang[3], Liang-Duan Liu[4,5,6], Qingfeng Zhu[1,7], Yun-Wei Yu[4,5,6], Keiichi Maeda[8], Lluís Galbany[9,10], Hanindyo Kuncarayakti[11,12], Željko Ivezić[13], Saurabh W. Jha[14], Peter Yoachim[13], Dezheng Meng[1,2], Weiyu Wu[1,2], Zhengyan Liu[1], Andrew J. Connolly[13], Zigao Dai[1], Ziqing Jia[1], Wen Zhao[1], Lulu Fan[1,7], Ming Liang[15], Hairen Wang[16], Jian Wang[7,17], and Hongfei Zhang[17]

[1] Department of Astronomy, University of Science and Technology of China, Hefei 230026, People's Republic of China; jian.jiang@ustc.edu.cn, zhuqf@ustc.edu.cn
[2] School of Astronomy and Space Sciences, University of Science and Technology of China, Hefei 230026, People's Republic of China
[3] National Astronomical Observatory of Japan, 2-21-1 Osawa, Mitaka, Tokyo 181-8588, Japan
[4] Institute of Astrophysics, Central China Normal University, Wuhan 430079, People's Republic of China
[5] Laboratory for Compact Object Astrophysics and Astronomical Technology, Central China Normal University, Wuhan 430079, People's Republic of China
[6] Education Research and Application Center, National Astronomical Data Center, Wuhan 430079, People's Republic of China
[7] Institute of Deep Space Sciences, Deep Space Exploration Laboratory, Hefei 230026, People's Republic of China
[8] Department of Astronomy, Kyoto University, Kitashirakawa-Oiwake-cho, Sakyo-ku, Kyoto 606-8502, Japan
[9] Institute of Space Sciences (ICE-CSIC), Campus UAB, Carrer de Can Magrans, s/n, E-08193 Barcelona, Spain
[10] Institut d'Estudis Espacials de Catalunya (IEEC), 08860, Castelldefels (Barcelona), Spain
[11] Tuorla Observatory, Department of Physics and Astronomy, FI-20014, University of Turku, Finland
[12] Finnish Centre for Astronomy with ESO (FINCA), FI-20014, University of Turku, Finland
[13] Department of Astronomy, University of Washington, Box 351580, Seattle, WA 98195-1580, USA
[14] Department of Physics and Astronomy, Rutgers, The State University of New Jersey, 136 Frelinghuysen Road, Piscataway, NJ 08854, USA
[15] National Optical Astronomy Observatory (NSF's National Optical-Infrared Astronomy Research Laboratory), 950 N Cherry Ave., Tucson, AZ 85726, USA
[16] Purple Mountain Observatory, Chinese Academy of Sciences, Nanjing 210023, People's Republic of China
[17] State Key Laboratory of Particle Detection and Electronics, University of Science and Technology of China, Hefei 230026, People's Republic of China
Received 2026 February 19; revised 2026 April 14; accepted 2026 April 25; published 2026 June 10

Abstract

We investigate the multiband photometric properties of seven supernovae (SNe) showing double-peaked light-curve evolution and prominent shock-cooling emission, observed by the Wide Field Survey Telescope during its first year of operation. By jointly employing an analytic early shock-cooling model and the Arnett radioactive-diffusion model, we fit the bolometric light curves and infer ejecta masses in the range 1.1–2.6 $M_\odot$, consistent with a transitional population between ultrastripped SNe and normal stripped-envelope SNe. The envelope masses are estimated to be $M_{\rm env} = 0.1$–$0.4\,M_\odot$, while the progenitors are constrained to be yellow or blue supergiants with radii of $R = 120$–$300\,R_\odot$. Using empirical relations, we estimate progenitor luminosities of $L = 10^{4.6}$–$10^{4.9}\,L_\odot$, corresponding to zero-age main-sequence masses of 8–20 $M_\odot$. Theoretical models suggest that such progenitors are more naturally produced through binary evolution channels, as single-star evolutionary pathways are unable to yield ejecta masses this low.

Unified Astronomy Thesaurus concepts: Supernovae (1668); Type Ib supernovae (1729); Type Ic supernovae (1730); Observational astronomy (1145); Core-collapse supernovae (304); Sky surveys (1464)

Materials only available in the online version of record: data behind figures

1. Introduction

Stellar evolution theory predicts that massive stars ($\gtrsim 8\,M_\odot$) experience core collapse at the end of their lives, exploding as core-collapse supernovae (CCSNe) and resulting in the formation of neutron stars or black holes (A. Gal-Yam 2017; H.-T. Janka 2012). Stripped-envelope supernovae (SESNe) constitute a major subset of CCSNe, representing the explosions of massive stars that have lost most or all of their H/He envelopes by the end of their lives due to binary interactions, stellar winds, or other physical mechanisms (S.-C. Yoon et al. 2017; Q. Fang et al. 2019; N.-C. Sun et al. 2023). Depending on the extent of envelope stripping, SESNe are spectroscopically classified into IIb → Ib → Ic with increasing degrees of stripping (A. Gal-Yam 2017; E. Karamehmetoglu et al. 2017; S. J. Prentice & P. A. Mazzali 2017).

A typical characteristic of many Type IIb SNe is their double-peaked light curves (e.g., SN 1993J—S. E. Woosley et al. 1994; SN 2016gkg—I. Arcavi et al. 2017, M. C. Bersten et al. 2018; SN 2017jgh—P. Armstrong et al. 2021; SN 2020bio—C. Pellegrino et al. 2023; SN 2021zby—Q. Wang et al. 2023; SN 2024abfo—A. Reguitti et al. 2025); among these, SN 2017jgh and SN 2021zby show a complete and prominent cooling peak due to the high cadence and long-term monitoring of Kepler telescope and TESS, but there was no sign of shock breakout (SBO) before the shock-cooling rise, probably due to the low brightness. Moreover, with the advent of wide-field surveys such as Asteroid Terrestrial-impact Last Alert System (ATLAS) and Zwicky Transient Facility (ZTF), an increasing number of Type Ib/c SNe have been found to show double-peaked light curves. These features are interpreted as signatures of the shock traversing circumstellar material (CSM) or envelope formed during binary interactions, wind, wave heating process, or pulsational pair-instability mechanisms, followed by subsequent cooling of the ejected material (K. K. Das et al. 2023, 2024; hereafter D23 and D24, respectively). Theoretically, the initial peak of the light curve is commonly attributed to the SBO, which marks the moment when the supernova (SN) shock wave—generated by the core bounce during collapse—breaks out from the surface of the progenitor star. This phenomenon produces a brief but intense flash of radiation, often considered as the first observable signal of a CCSN. The duration of the SBO is extremely short, typically lasting from seconds to hours (E. Waxman & B. Katz 2017). As a result, detecting this phase poses significant observational challenges.

Following the SBO, the early-time light-curve evolution is dominated by the shock-cooling emission, which arises as the outer layers of the ejecta heated by the shock and cool down adiabatically. This phase typically manifests as a relatively rapid decline in brightness over the first few days after explosion. The detailed morphology of this early peak—including its timing, duration, and luminosity—carries valuable information about the structure and extent of the progenitor's outer envelope (A. L. Piro et al. 2021; hereafter P21). Therefore, efforts to detect and characterize the early rise and decline of the light curve are crucial for constraining the final evolutionary stages of massive stars and improving our understanding of the pre-SN mass-loss processes. In this paper, we investigate SNe with early-excess emission discovered in the first year of the Wide Field Survey Telescope (WFST) operation, fitting their light curves to constrain progenitor properties and possible evolutionary origins.

This paper is organized as follows. The observation and data reduction are presented in Section 2, followed by the analysis in Section 3, where photometric properties are analyzed. The analytical modeling of the early-phase light curves and the explosion parameters are presented in Section 4, and finally, the results are discussed and summarized in Section 5.

2. Observations and Data Reduction

WFST (T. Wang et al. 2023)[18] is a 2.5 m optical telescope with a 6.5 deg^2 field of view and high *u*-band sensitivity, jointly developed by the University of Science and Technology of China and the Purple Mountain Observatory. Its design enables deep, wide surveys of the northern sky, making it well suited for probing the dynamic universe and discovering extragalactic transients such as SNe and tidal disruption events. WFST commenced a pilot survey ("WFST-PS") from 2024 March 4 to July 10 and started the 6 yr time-domain survey on 2024 December 14.

A total of 2800 SN candidates have been discovered by the Deep High-cadence *ugr*-band Survey project (DH*ugr;* J.-a. Jiang et al. 2026, in preparation), a key project for both pilot and formal surveys, as of 2025 June 30. The primary observing strategy involved daily/hourly cadence photometries in *u*-, *g*-, and *r*-bands.[19] The photometric data were derived using the WFST data pipeline, based on the Large Synoptic Survey Telescope software stack (T. Axelrod et al. 2010; J. Bosch et al. 2018; Ž. Ivezić et al. 2019). Host-galaxy spectra are available for approximately 400 candidates; the majority of the sample relies on photometric redshift determinations. WFST provided initial detections for most targets.

All 2800 light curves underwent comprehensive visual inspection, and 56 candidates were identified with clear double-peaked signature. These early peaks likely originate from shock-cooling emission, and such features suggest extended progenitor envelopes or interactions with CSM. The following selection criteria were subsequently applied to this subset:

1. A minimum of five photometric measurements is required. These data must be obtained within 10 days of the initial detection.
2. A distinct fading phase must precede the secondary rebrightening. Measurements during the decline were verified manually. Science images were inspected to ensure data validity.
3. A reliable host spectroscopic redshift is mandatory for all candidates.
4. Early light-curve evolution must be detected in at least two bands. This includes the initial rise or decline.

Seven SNe are ultimately selected as the final sample for detailed analysis. The properties of all samples are shown in Table 1. All SNe except WFST250617iqnc and WFST-PS240307bn are solely discovered by WFST. ZTF detected WFST250617iqnc at MJD 60821.27 with a *g*-band magnitude of 20.009 ± 0.163. This is approximately 0.40 days earlier than the first WFST detection (MJD 60821.67). However, the brightness variation between the two observation epochs is about 0.016 mag, which is significantly smaller than the ZTF measurement error. Therefore, the impact of this earlier detection on the overall trend of the light curve is negligible. On the other hand, ATLAS detections of WFST-PS240307bn near the major peak were not used in the subsequent calculation and analysis due to a large scatter of the ATLAS photometric results.

Direct spectroscopic classification is precluded by the faint apparent magnitudes of the samples. This limitation persists even at peak phases (fainter than 20 mag in most SNe). Consequently, all redshifts are derived from host-galaxy spectra provided by the Dark Energy Spectroscopic Instrument (DESI; DESI Collaboration et al. 2026). Nondetection constraints are absent for WFST-PS240307bn and WFST250521xflp. These targets were detected during the commencement of WFST operations. Peak magnitudes in the *r*-band were derived via Gaussian process (GP) regression, and the full light curve was utilized for this fitting. Discovery magnitudes of all SNe are in the *g*-band range primarily from 19.3 to 22.0 mag.

2.1. Extinction Correction

Interstellar dust extinction affects the observed properties of SNe; therefore, accurate extinction correction is essential for linking observations with theoretical models. The total extinction is composed of two components: Galactic extinction from the Milky Way and host-galaxy extinction arising from the local environment of the SN. Galactic extinction is corrected using the reddening maps of E. F. Schlafly & D. P. Finkbeiner (2011), with extinction coefficients calculated according to the extinction law of J. A. Cardelli et al. (1989). We adopt a standard interstellar medium extinction model with $R_V = 3.1$ throughout this work.

[18] https://wfst.ustc.edu.cn

[19] However, due to an unexpected technical issue of the filter-exchange system that occurred in late 2024 March, only *g*- and *r*-band data were obtained during the remaining WFST-PS period.

Table 1
Properties of WFST SCE SNe

Name	IAU Name (AT)	R.A.	Decl.	Redshift[a]	$E(B-V)_{\mathrm{MW}}$[b] (mag)	r_{peak} Mag.[c] (mag)	Offset (arcsec)
WFST-PS240307bn	2024emy	$11^h14^m18\overset{s}{.}0$	$-00^d20^m28\overset{s}{.}2$	0.039	0.031	-16.76 ± 0.01	2.71
WFST-PS240307bh	2024tfn	$14^h14^m15\overset{s}{.}0$	$+04^d30^m46\overset{s}{.}9$	0.076	0.022	-19.02 ± 0.01	0.29
WFST-PS240503d	2024tna	$13^h39^m36\overset{s}{.}6$	$+04^d45^m39\overset{s}{.}9$	0.085	0.026	-17.25 ± 0.15	2.74
WFST250521xflp	2025eer	$13^h09^m03\overset{s}{.}2$	$-00^d03^m07\overset{s}{.}6$	0.081	0.021	-16.66 ± 0.03	5.40
WFST250522otkg	2025dsj	$11^h03^m35\overset{s}{.}4$	$+03^d20^m00\overset{s}{.}.6$	0.053	0.054	-15.95 ± 0.05	14.17
WFST250605fjov	2025lbe	$13^h30^m11\overset{s}{.}5$	$+01^d51^m41\overset{s}{.}9$	0.083	0.022	-17.28 ± 0.04	2.08
WFST250617iqnc	2025mba	$13^h17^m05\overset{s}{.}3$	$+01^d49^m46\overset{s}{.}.4$	0.036	0.031	-15.47 ± 0.04	3.78

Notes.
[a] Spectroscopic redshift of the host galaxy described in Section 2.3.
[b] Galactic extinction derived from dust maps provided by E. F. Schlafly & D. P. Finkbeiner (2011).
[c] r-band peak apparent magnitude of the main peak.

Spectroscopic observations are unavailable for the current sample. Consequently, host-galaxy reddening is estimated by comparing SN colors with templates (see Section 3.1). Comparison indicates that host-galaxy reddening is minimal. Furthermore, most SNe are located at large offsets ($>2''$) from their host centers. Host-galaxy extinction is therefore neglected in this analysis.

2.2. Light Curve

Multiband light curves for the entire sample are presented in Figure 1, where data are corrected for extinction. Available 3σ nondetections are included.

The observational frame is used in the figure, and a time dilation effect correction is applied to the absolute magnitude as follows:

$$M_{\mathrm{corr}} = M + 2.5 \times \log_{10}(1 + z). \tag{1}$$

Here z denotes the redshift, accounting for corrections due to cosmological time dilation. A flat ΛCDM cosmology is adopted throughout this work. The Hubble constant is set to $H_0 = 67.66$ km s^{-1} Mpc^{-1}, and the matter density parameter is $\Omega_m = 0.3111$ (Planck Collaboration et al. 2018). These values are utilized for all luminosity distance calculations and corrections.

The sample SNe show a rapid early decline within days of discovery followed by a luminous second peak (decline rates in g- and r-bands were derived for the seven sources over a ∼3 day rest-frame period; Table 2). Notably, WFST250522otkg and WFST250605fjov were detected prior to the first maximum. These observations trace the surface heating and expansion driven by the shock wave propagating through the hydrogen envelope, as well as the subsequent spectral evolution where the cooling blackbody peak shifts through the observed bands. WFST-PS240307bh lacks dense sampling during the cooling phase, but its tight nondetection limits effectively constrain the early evolution.

WFST250521xflp shows the steepest decline with a magnitude drop of 2.12 ± 0.32 mag over 2.80 days, corresponding to a rate of 0.76 ± 0.13 mag day^{-1}. In contrast, WFST250605fjov shows the slowest evolution with a rate of approximately 0.05 ± 0.02 mag day^{-1}.

For comparison, SN 2016gkg features a $V(R)$-band decline rate of 0.68 ± 0.06 (0.66 ± 0.10) mag day^{-1} (M. C. Bersten et al. 2018). This value falls within the range of the current sample, suggesting a common physical origin for the emission. Late-time evolution is generally unobserved due to the faintness and high redshift of the sources. Consequently, the ^{56}Ni-powered radioactive tail remains unconstrained. However, this absence does not affect the analysis of the primary shock-cooling mechanism.

2.3. Host

Host spectra are obtained from Data Release 1 of DESI. DESI is a large-scale redshift survey targeting galaxies and quasars over 14,000 deg^2 of the extragalactic sky, providing high-precision redshifts that enable robust host-galaxy identification and distance measurements for SNe. Besides, host galaxies are matched from Data Release 16 of the Sloan Digital Sky Survey (SDSS), the fourth data release of the fourth phase of SDSS (M. R. Blanton et al. 2017). A positional crossmatch is performed using coordinates of SNe to identify the nearest galaxy in projection and obtain their spectrums for further analysis. A total of 19 host-galaxy spectra are secured, with at least 1 per SN. Multiple spectra for the same source show consistent redshifts and similar spectral morphologies.

Host spectra are fitted using the Python package Bayesian Analysis of Galaxies for Physical Inference and Parameter EStimation (BAGPIPES; A. C. Carnall et al. 2018).[20] This package performs Bayesian spectral energy distribution (SED) analysis. The `MultiNest` algorithm is employed for parameter space exploration (F. Feroz et al. 2009). It provides posterior distributions and Bayesian evidence. Further modeling details are in A. C. Carnall et al. (2019). Best-fit results are presented in Table 3.

3. Analysis

3.1. Photometric Comparisons

Figure 2 shows the comparison of absolute r- and R-band light curves between sample SNe and other well-studied SESNe.

WFST-PS240307bh represents the brightest object across all evolutionary phases. It shows an r-band peak absolute magnitude of −19.02, consistent with the Type Ib/c SN 2020bvc. Their light-curve morphologies align closely from −10 to 40 days. However, SN 2020bvc presents a faster decline after 50 days, likely attributable to UV leakage. In addition to WFST-PS240307bh, the brightness of the first peak is comparable or

[20] https://bagpipes.readthedocs.io

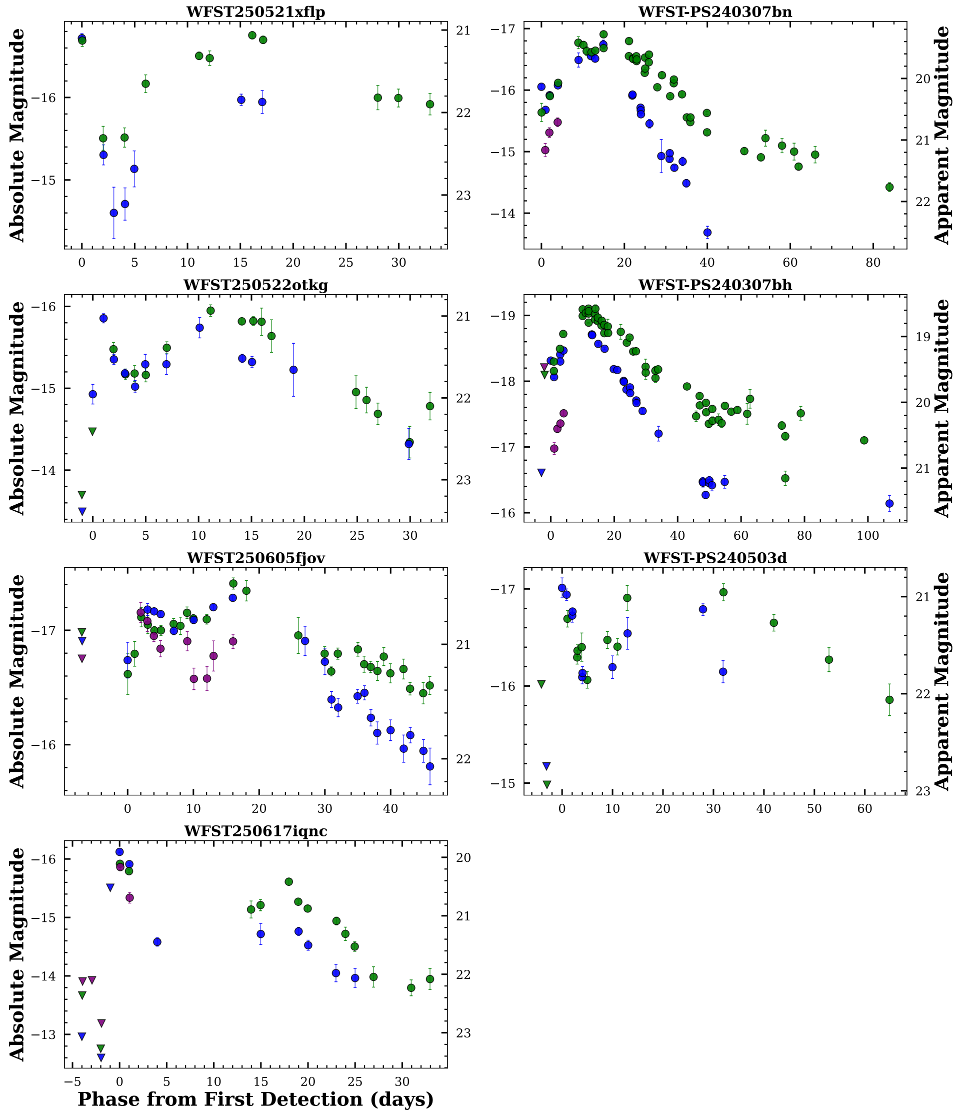

Figure 1. Multiband light curves are presented for the full sample. The g-band data are shown in blue, and green and purple symbols denote r- and u-bands, respectively. Triangles indicate 3σ upper limits. Nondetections separated by >7 days from the first detection are omitted. All light curves have been corrected by the Milky Way (MW) extinction only.

(The data used to create this figure are available in the online article.)

even higher than that of the second peak for the other six SNe. We note that although the second peak of WFST-PS240307bh is comparable to the peak of normal Type Ia SNe, the brightness of <-18.2 mag for the first g-band peak is too high for any early-excess scenario of Type Ia SNe (J.-a. Jiang et al. 2017, 2018; K. Maeda et al. 2018). WFST250605fjov and WFST-PS240503d resemble SN 2016gkg and SN 2011dh around the primary peak. Their peak magnitudes are -17.32 and -16.99, respectively. These values align with SN 2016gkg (-17.56) and SN 2011dh (-17.34) in the R-band.

WFST-PS240503d resembles SN 2016gkg during the shock-cooling phase. Conversely, WFST250605fjov displays a shorter interval between the first and primary peaks, indicating a more rapid evolution. WFST250521xflp displays brightness and evolution comparable to SN 2022hnt when excluding the shock-cooling phase. Notably, WFST250521xflp shows the steepest decline during shock cooling, which likely stems from low envelope and ejecta masses.

WFST250522otkg and WFST250617iqnc represent the faintest SNe in the sample. Although SN 2021inl appears even fainter across all phases, it shows a slightly slower decline rate compared to the WFST targets, as shown in Figure 3. This discrepancy is attributed to redshift effects, as the observed band corresponds to bluer rest-frame wavelengths characterized by faster theoretical evolution.

$g-r$ color evolution between WFST SN sample and SN 2016gkg is shown in Figure 4. While some targets have limited multiband observations, resulting in fewer data points, the overall color trends are broadly consistent with SN 2016gkg.

During the early phases, the $g-r$ color typically evolves from blue to red due to shock cooling. However, WFST0605fjov initially presents a blueward trend before rapidly reddening, indicating a temperature increase during its early phase. The $g-r$ color then undergoes another red-to-blue transformation because of the second peak powered by the decay of ^{56}Ni subsequently turning to the red tail.

Table 2
Shock Cooling Decline Rate in *r*- and *g*-band of WFST SCE SNe

Name	Decline Start (MJD)	Decline End (MJD)	Δm (mag)	Decline Rate (mag day^{-1})
WFST-PS240503d	60432.74	60436.80	0.88 ± 0.12	0.23 ± 0.03
WFST250521xflp	60725.76	60728.79	2.12 ± 0.32	0.76 ± 0.11
WFST250522otkg	60727.72	60730.70	0.84 ± 0.09	0.30 ± 0.03
WFST250605fjov	60812.71	60816.71	0.19 ± 0.06	0.05 ± 0.02
WFST250617iqnc	60821.67	60825.67	1.54 ± 0.07	0.40 ± 0.02
WFST-PS240307bh	60386.83	60387.86	0.25 ± 0.03	0.26 ± 0.03
WFST-PS240307bn	60375.70	60376.70	0.38 ± 0.04	0.39 ± 0.04

Note: WFST-PS240307bh and WFST-PS240307bn possess fewer than two *r*-band detections during shock cooling. Consequently, *g*-band light curves are utilized for decline rate determinations. Values are derived directly from the photometric measurements.

The $g - r$ color templates of Type IIb and Ib/c SNe are shown in the figure. They were derived from comprehensive statistical studies of SESN light curves, which show remarkably uniform color evolution during the early post-maximum phase (Ó. Rodríguez et al. 2023). The uniformity spans 0 to ~20 days relative to the *V*-band maximum. To estimate host extinction, we fit the observed $g - r$ colors using GP regression and compare them with the Type IIb SN template. Any positive color excess is converted to $E(B - V)_{\rm host}$ using an empirical coefficient of $k = 0.98$ (E. F. Schlafly & D. P. Finkbeiner 2011). Most of our SNe appear bluer than the template, implying $E(B - V)_{\rm host} \sim 0$. For the remaining three SNe, WFST250521xflp lacks sufficient data coverage for a reliable calculation, while WFST-PS240503d and WFST-PS240307bn yield statistically insignificant (0.140 ± 0.221 mag) and negligible (0.103 ± 0.041 mag) values, respectively. Given the overall uncertainties introduced by these estimations, host-extinction corrections were not applied for our sample.

3.2. Bolometric Light Curve

Bolometric light curves were derived using `SuperBol` (M. Nicholl 2018), which accepts extinction-corrected apparent magnitudes. Pseudobolometric fluxes were computed by fitting blackbody SEDs, integrating the flux over the full SED at each epoch.

Since detections are primarily limited to *g*- and *r*-bands, the lack of multiband constraints introduces potential uncertainties. High-order polynomial interpolations were applied to mitigate this issue, with the fitting order dependent on temporal coverage and data quality. *g*-band light curves were interpolated to the reference epochs defined by the better-sampled *r*-band.

WFST-PS240307bh, WFST250605fjov, and WFST-PS240307bn possess early-phase *u*-band detections, providing improved constraints on the SED fitting. Consequently, the analysis treated sources with and without *u*-band data separately. A blackbody SED was fitted for each epoch.[21] Bolometric luminosities were derived alongside blackbody temperatures. The resulting bolometric light curves and temperature evolution are presented in Figure 5.

A temporal validity cut is applied based on a temperature threshold of 8120 K (0.7 eV), following the criterion of N. Sapir & E. Waxman (2017; hereafter SW17). Temperature fitting errors are omitted from the figure because `SuperBol` cannot compute uncertainties with only two bands. Consequently, the independent approach of L. Martinez et al. (2022) is utilized to verify the results. This method employs empirical correlations between bolometric corrections and colors, using $g - r$ to derive the necessary corrections.

The evolution is typically modeled in three phases: cooling, main peak, and tail. However, the current light curves do not extend to the tail phase, which usually begins ~100 days postexplosion. Therefore, this phase is excluded from the analysis. The remaining cooling and main peak phases are distinguished by the 8120 K boundary. Given the results from two methods are close, the interpolated data are utilized for the analysis.

3.3. ^{56}Ni-powered Light-curve Modeling

Physical parameters including the ^{56}Ni mass, ejecta mass, and kinetic energy are derived from the radioactively powered second light-curve peaks. We employ the analytic model introduced by W. D. Arnett (1982) to relate the observed bolometric light curves to the radioactive energy deposition from the $^{56}{\rm Ni} \longrightarrow {}^{56}{\rm Co} \longrightarrow {}^{56}{\rm Fe}$ decay chain.

Although originally developed for Type Ia SNe, this framework has been widely applied to SESNe owing to the shared ^{56}Ni-powered peak mechanism. Our approach is consistent with established applications in the literature (J. D. Lyman et al. 2016; F. Taddia et al. 2018; Y. Dong et al. 2024).

The model assumes homologous, spherically symmetric expansion with constant, time-independent optical opacity. The ^{56}Ni distribution is treated as a centrally concentrated, point-like source with a negligible initial radius. Under these assumptions, the bolometric luminosity is expressed as a function of the ejecta mass $M_{\rm ej}$, kinetic energy E_k, and synthesized ^{56}Ni mass $M_{\rm Ni}$.

Specifically, the radioactive-powered luminosity prior to γ-ray leakage is explicitly formulated as

$$L_{\rm rad}(t) = \frac{2M_{\rm Ni}}{\tau_m}\exp(-t^2/\tau_m^2)\int_0^t \exp(t'^2/\tau_m^2)\frac{t'}{\tau_m} \times [(\epsilon_{\rm Ni} - \epsilon_{\rm Co})\exp(-t'/\tau_{\rm Ni}) + \epsilon_{\rm Co}\exp(-t'/\tau_{\rm Co})]dt', \quad (2)$$

where $\epsilon_{\rm Ni} = 3.9 \times 10^{10}$ erg s^{-1} g^{-1} and $\epsilon_{\rm Co} = 6.8 \times 10^9$ erg s^{-1} g^{-1} are the specific heating rates and $\tau_{\rm Ni} = 8.8$ days and $\tau_{\rm Co} = 111.3$ days are the e-folding decay timescales for ^{56}Ni and ^{56}Co, respectively (A. Clocchiatti & J. C. Wheeler 1997). The

[21] Early-phase SED fittings are given in Figure A1 for reference.

Table 3
Host Properties of WFST SCE SNe

Name	log(SFR) ($M_\odot$ yr^{-1})	log(Stellar Mass) ($M_\odot$)	A_v (mag)	Age (Gyr)	Metallicity ($Z_\odot$)
WFST-PS240307bn	$-2.27^{+0.03}_{-0.03}$	$8.05^{+0.04}_{-0.04}$	$0.11^{+0.07}_{-0.07}$	$2.63^{+0.66}_{-0.50}$	$0.12^{+0.02}_{-0.02}$
WFST-PS240307bh	$-0.88^{+0.01}_{-0.01}$	$9.77^{+0.00}_{-0.00}$	$0.54^{+0.00}_{-0.00}$	$1.72^{+0.01}_{-0.00}$	$1.55^{+0.02}_{-0.02}$
WFST-PS240503d	$-0.68^{+0.01}_{-0.01}$	$8.96^{+0.01}_{-0.01}$	$0.05^{+0.06}_{-0.03}$	$1.24^{+0.06}_{-0.06}$	$1.66^{+0.08}_{-0.06}$
WFST250522otkg	$-0.40^{+0.00}_{-0.01}$	$10.27^{+0.00}_{-0.00}$	$0.83^{+0.01}_{-0.01}$	$2.70^{+0.06}_{-0.06}$	$1.90^{+0.03}_{-0.03}$
WFST250521xflp	$-0.58^{+0.00}_{-0.00}$	$9.47^{+0.00}_{-0.00}$	$0.51^{+0.02}_{-0.02}$	$1.32^{+0.04}_{-0.02}$	$1.90^{+0.05}_{-0.05}$
WFST250605fjov	$-1.54^{+0.02}_{-0.03}$	$8.43^{+0.04}_{-0.02}$	$0.10^{+0.07}_{-0.06}$	$1.54^{+0.27}_{-0.20}$	$0.16^{+0.01}_{-0.01}$
WFST250617iqnc	$-0.73^{+0.00}_{-0.01}$	$9.42^{+0.01}_{-0.01}$	$0.76^{+0.03}_{-0.02}$	$3.30^{+0.22}_{-0.20}$	$2.29^{+0.02}_{-0.02}$

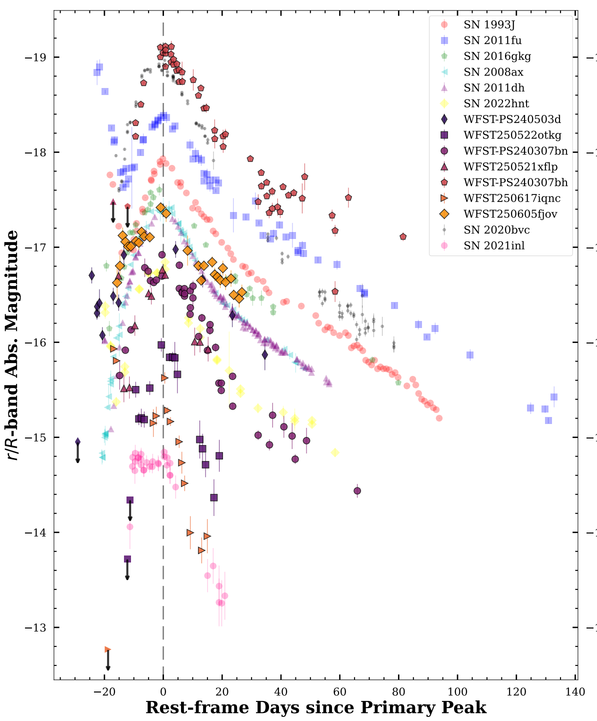

Figure 2. Light curves in r-/R-band absolute magnitude of all SNe. For comparison, light curves of several well-studied SNe are plotted. Gray dashed line marks the phase of primary peak.

effective diffusion timescale τ_m is defined as

$$\tau_m = \left(\frac{2\kappa_{\rm opt} M_{\rm ej}}{\beta c v_{\rm sc}}\right)^{1/2}, \tag{3}$$

with $\beta = 13.8$ being an integration constant. Furthermore, to account for the incomplete trapping of γ-rays at late phases, the final deposited luminosity is modified by a leakage term, yielding

$$L(t) = L_{\rm rad}(t)(1 - e^{-\tau_\gamma(t)}), \tag{4}$$

with the γ-ray optical depth defined as $\tau_\gamma(t) = \frac{3\kappa_\gamma M_{\rm ej}}{4\pi v_{\rm sc}^2 t^2}$. The γ-ray opacity κ_γ is treated as a free parameter in our fitting routine.

3.4. Shock-cooling Light-curve Modeling

Analytic models for shock-cooling emission differ primarily in their treatment of the envelope geometry and density structure. Representative formulations include those of SW17 and P21. The P21 model explicitly distinguishes between outer and inner envelope regions, highlighting a sensitivity to the polytropic index. In contrast, SW17 demonstrated that shock-cooling emission is relatively insensitive to this index and shows only a weak dependence on the progenitor's density structure. Initial tests using the SW17 prescription result in systematically poorer fits to our dataset. Due to the lack of early u-band observations, poorly constrained early-time temperatures lead to exceptionally large Markov Chain Monte Carlo fitting errors. We therefore adopt the P21 model to describe the shock-cooling phase, while the secondary radioactive-powered peak is modeled using the Arnett formalism described in Section 3.3, The two components are separated by the temperature cut (8120 K) shown in Figure 5.

To describe the full double-peaked light curves, we employ a combined framework in which the total flux is computed as the sum of the shock-cooling and radioactive components.

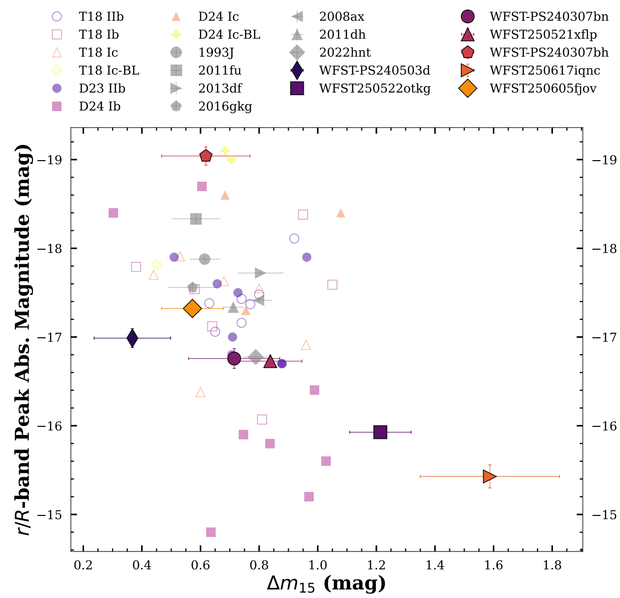

Figure 3. The light-curve decline rate Δm_{15} is plotted against peak brightness. Values correspond to the r- or R-band. The R-band is adopted for SN 1993J, SN 2011fu, and SN 2013df. SN 2016gkg, SN 2008ax, and SN 2011dh also utilize this band. All other sources rely on r-band observations. Comparison samples include SESNe from F. Taddia et al. (2018), D23, and D24. WFST-PS240307bh shows a peak brightness and decline rate comparable to broad-lined Type Ic (Type Ic-BL) SNe. Faster declining light curves generally possess lower peak luminosities. This trend associates high Δm_{15} values with fainter magnitudes. WFST250522otkg and WFST250617iqnc display the highest decline rates. However, these measurements carry large uncertainties.

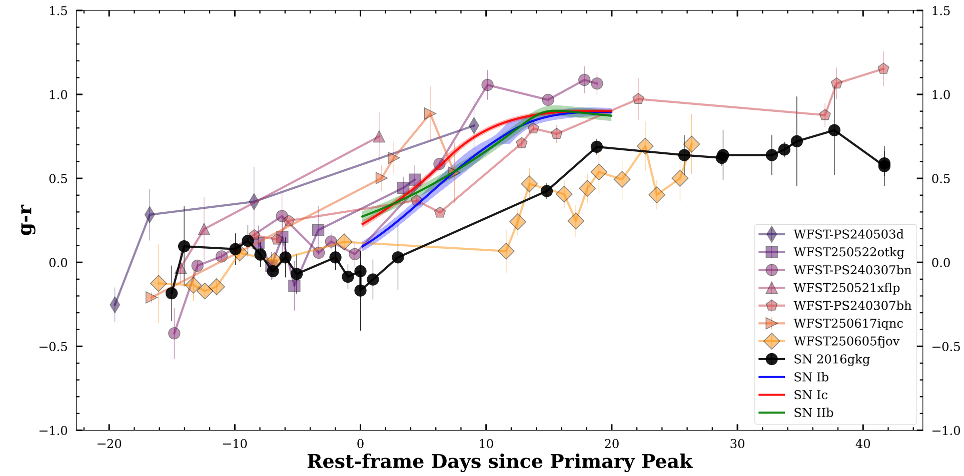

Figure 4. Color evolution of SNe compared to SN 2016gkg, where the $V-R$ color of SN 2016gkg is transformed to $g-r$ using the empirical color–color relation calibrated by K. Jordi et al. (2006). The solid lines with error range coded by colors are color evolution templates from the main peak to 20 days after the rest frames of Type IIb, Ib, and Ic SNe introduced in M. D. Stritzinger et al. (2018).

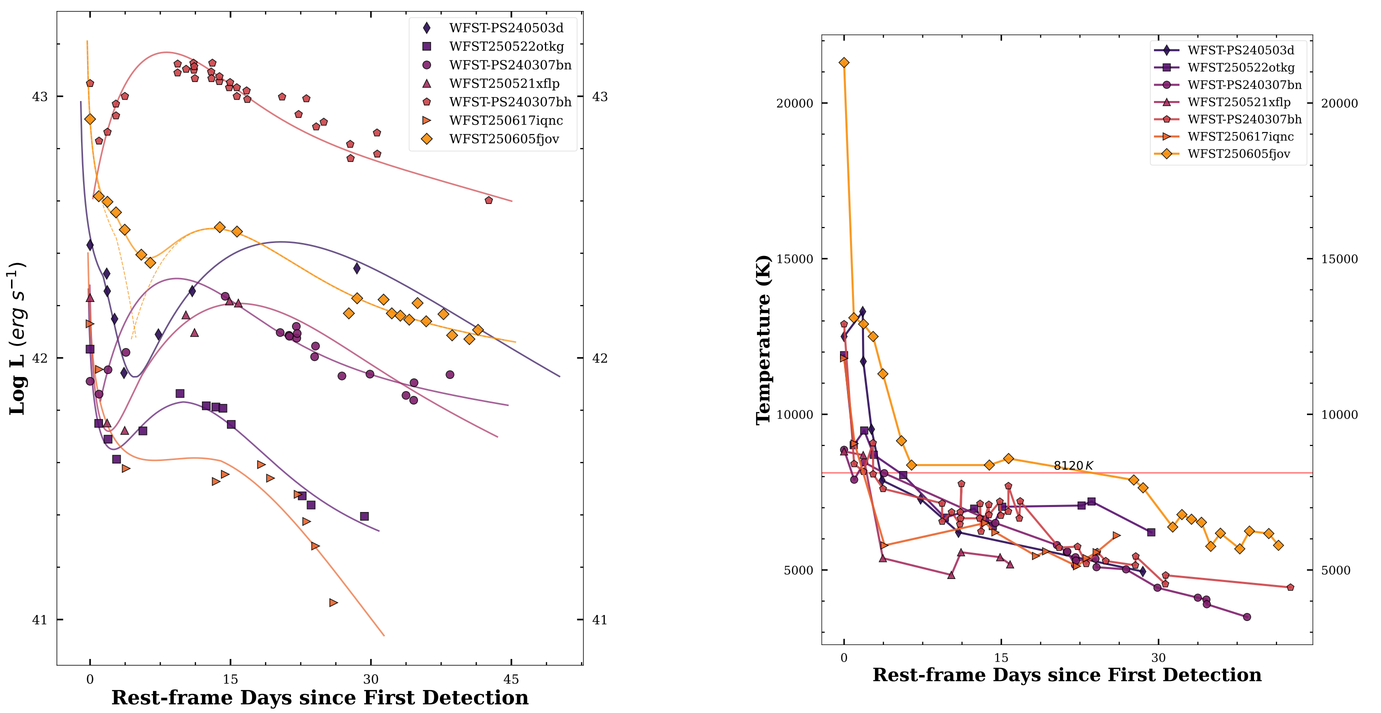

Figure 5. Left: the bolometric light curves of SNe. Solid lines denote the total best fits from the Arnett and P21 model, with dotted lines showing the decomposed components for a representative example. Right: blackbody temperature evolution of SNe derived from `SuperBol` fitting. Shock-cooling models are valid only for data where the $T_{\rm BB}$ is greater than 8120 K or 0.7 eV (SW17).

(The data used to create this figure are available in the online article.)

Although these components are often fitted independently in the literature (L. Chen et al. 2025; B. M. Subrayan et al. 2025), we perform a simultaneous fit in order to reduce parameter degeneracies.

A common optical opacity is enforced for both components. Because our sample lacks direct spectroscopic classifications, the true ejecta composition may range from Type IIb SNe retaining a small amount of hydrogen to more strongly stripped Type Ib/c SNe. We therefore adopt a broad uniform prior of $\kappa_{\rm opt} = 0.05$–$0.3\ {\rm cm^2\ g^{-1}}$ to reflect this uncertainty. It is worth noting that this represents an effective gray opacity within the semianalytic model rather than a true time- and wavelength-dependent microscopic opacity. Consequently, the inferred physical parameters remain partially degenerate with the adopted $\kappa_{\rm opt}$. The best-fit parameters are summarized in Table 4, and the corresponding bolometric light-curve fits are shown in Figure 5.

We note that more general modeling frameworks that explicitly solve the time-dependent radiative diffusion equation and self-consistently track the transition from shock-cooling emission to radioactive heating have recently been developed in the literature (e.g., `TransFit`; L.-D. Liu et al. 2025). However, given the limited temporal coverage and signal-to-noise ratio of the early-time data in our sample, we

Table 4
Best Parameters of Explosion from Fitting

Name	$M_{\rm env}$ ($M_\odot$)	$R_{\rm env}$ ($R_\odot$)	$M_{\rm ej}$ ($M_\odot$)	$M_{\rm Ni}$ ($M_\odot$)	E_k (10^{51} erg)
WFST-PS240503d	$0.08^{+0.31}_{-0.02}$	$122.47^{+230.13}_{-41.90}$	$2.57^{+0.76}_{-0.41}$	$0.22^{+0.03}_{-0.04}$	$3.95^{+0.75}_{-1.27}$
WFST-PS240307bn	…	…	$1.17^{+0.63}_{-0.46}$	$0.07^{+0.00}_{-0.00}$	$0.86^{+1.53}_{-0.65}$
WFST-PS240307bh	…	…	$1.19^{+0.40}_{-0.49}$	$0.49^{+0.00}_{-0.00}$	$1.57^{+1.60}_{-1.11}$
WFST250521xflp	$0.33^{+0.09}_{-0.15}$	$67.04^{+73.47}_{-25.17}$	$1.54^{+0.69}_{-0.61}$	$0.07^{+0.01}_{-0.01}$	$2.80^{+1.69}_{-1.68}$
WFST250522otkg	$0.42^{+0.06}_{-0.13}$	$257.24^{+153.32}_{-119.06}$	$1.09^{+0.46}_{-0.49}$	$0.02^{+0.00}_{-0.00}$	$2.18^{+1.73}_{-1.73}$
WFST250605fjov	$0.23^{+0.08}_{-0.06}$	$188.61^{+180.87}_{-63.35}$	$1.68^{+0.65}_{-0.58}$	$0.12^{+0.00}_{-0.00}$	$1.76^{+2.27}_{-1.11}$
WFST250617iqnc	$0.42^{+0.05}_{-0.09}$	$300.25^{+134.90}_{-76.01}$	$1.18^{+0.49}_{-0.21}$	$0.01^{+0.00}_{-0.00}$	$2.97^{+1.48}_{-1.37}$

Note. Reliable constraints on $M_{\rm env}$ and $R_{\rm env}$ could not be derived for WFST-PS240307bn and WFST-PS240307bh. The extremely brief duration of the shock-cooling phase in these events precluded robust fitting.

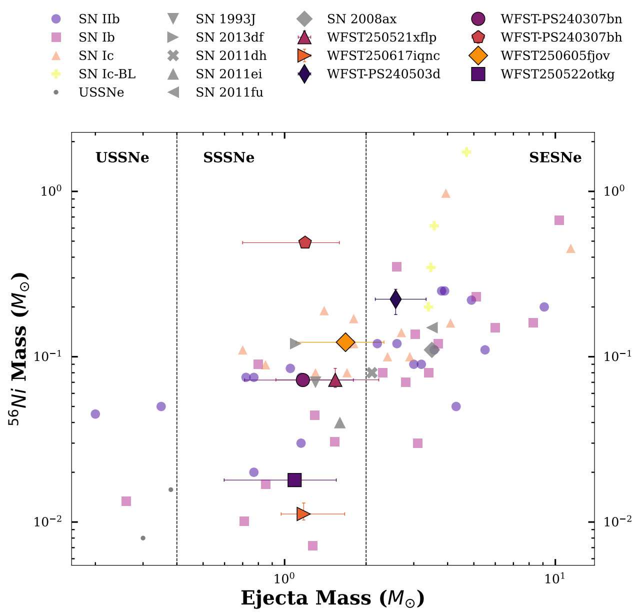

Figure 6. Best fit of ejecta mass versus nickel mass of SNe from the Arnett model; well-studied Type IIb SNe and SESNe are plotted for comparison.

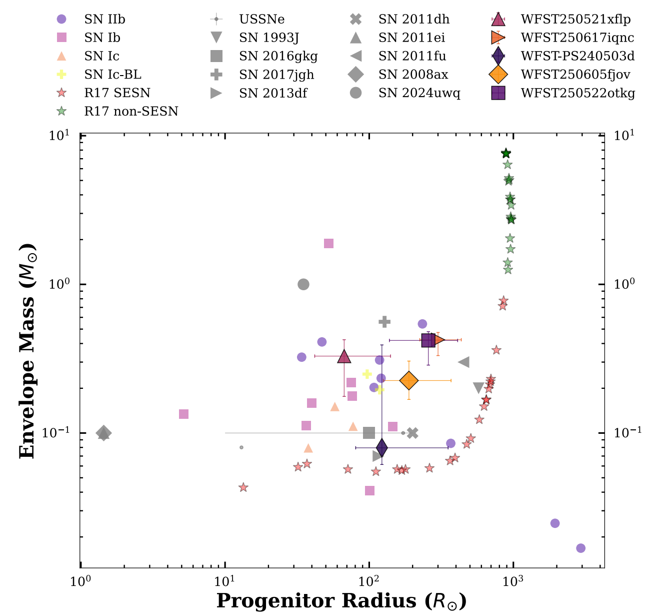

Figure 7. Progenitor radius versus envelope mass of SNe; well-studied Type IIb SNe and SESNe with progenitor parameters are plotted for comparison.

adopt the widely used analytic prescription of P21, which captures the dominant physical dependencies while introducing only a minimal number of free parameters.

4. Discussion

We place explosion and progenitor parameters derived from modeling in the context of well-studied SESNe to investigate correlations between key physical properties. This comparison allows us to assess the location of our sample in the parameter space and to probe for any distinctive characteristics that may shed light on progenitor diversity or explosion mechanisms.

4.1. Physical Parameters

Ejecta masses and ^{56}Ni masses for the sample SNe are presented in Figure 6, alongside comparative data for SESNe from F. Taddia et al. (2018), D23, and D24. Additionally, two ultrastripped-envelope SNe (USSNe) from K. De et al. (2018) and Y. Yao et al. (2020) are included.

Most events cluster within a moderate ejecta mass region of 0.4–2 $M_\odot$, consistent with the transitional type between USSNe and SESNe described in D23, characterized by strongly stripped envelopes. WFST-PS240503d represents the sole exception, showing the highest ejecta mass of $\sim$2.6 $M_\odot$.

Progenitor radii are plotted against envelope masses in Figure 7. The derived envelope masses range from 0.07 to 0.5 $M_\odot$, while radii span 60–300 $R_\odot$. These properties suggest yellow supergiant or blue supergiant progenitors, with hydrogen envelopes stripped via single-star winds or binary mass transfer.

Theoretical predictions for Type IIb SN envelope masses and radii from R. Ouchi & K. Maeda (2017; hereafter R17) are also displayed for comparison; these were computed using the MESA code under a binary evolutionary channel assumption. At fixed envelope masses, the current sample consistently yields more compact progenitor radii compared to these predictions. This discrepancy is likely attributable to convection efficiency: as noted by L. Dessart et al. (2013), efficient convection yields compact progenitors, whereas small mixing length parameters in models may result in overestimated radii. Additionally, the fact that R17 fixes the initial primary mass at 16 $M_\odot$ may account for the difference.

4.2. Constraining Progenitor Luminosity

Given that our sample lacks direct pre-explosion imaging, the progenitor luminosity cannot be independently constrained from observations. However, while the mapping between helium core mass and zero-age main-sequence mass depends sensitively on the choice of stellar evolution code, including MESA (Q. Fang & K. Maeda 2023; D. Temaj et al. 2024), KEPLER (T. Sukhbold et al. 2016, 2018), and HOSHI (K. Takahashi et al. 2023; Q. Fang et al. 2025b), the relationship between helium core mass and progenitor luminosity is found to be comparatively robust and largely independent of the adopted stellar model (Q. Fang et al. 2025b). This theoretical consistency provides an indirect method to estimate progenitor luminosities.

To estimate the helium core mass ($M_{\mathrm{He,core}}$), we assume that the total pre-explosion mass can be approximated as the sum of the derived ejecta mass (M_{ej}) and a canonical compact remnant (neutron star) mass of 1.4 $M_{\odot}$. Given that these events are likely Type IIb SNe, the residual hydrogen envelope mass is expected to be negligible compared to the total mass budget. Furthermore, the presence of this residual hydrogen implies that the progenitor star did not undergo significant helium stripping prior to explosion (M. R. Drout et al. 2023). Thus, we can approximate $M_{\mathrm{He,core}} \approx M_{\mathrm{ej}} + 1.4\,M_{\odot}$. The progenitor luminosities are then inferred from these core masses using the approximately universal empirical relation:

$$\log \frac{L}{L_{\odot}} = 1.47 \times \log \frac{M_{\mathrm{He,core}}}{M_{\odot}} + 4.01. \quad (5)$$

The cumulative distribution functions (CDFs) of the inferred progenitor luminosities for the SESNe samples from D23, D24, and F. Taddia et al. (2018) are shown in Figure 8. The progenitor luminosity distribution for Type II SNe from Q. Fang et al. (2025a) is included for comparison; these values were constrained using nebular spectroscopy. To construct the CDF, luminosities were sampled from an asymmetric Gaussian distribution defined by literature means and uncertainties. This process was iterated 10,000 times to minimize statistical noise. Solid lines and shaded regions denote the median and 68% confidence intervals, respectively. The positions of the current sample are marked with downward arrows, showing luminosities ranging from $\sim 10^{4.6}$ to $\sim 10^{4.9}\,L_{\odot}$.

The distributions of Type II SNe and SESNe are similar at low luminosities ($L \lesssim 10^{5.25}\,L_{\odot}$), whereas SESNe extend to higher luminosities ($L \lesssim 10^{5.75}\,L_{\odot}$). The progenitor luminosities of the current sample fall between the Type II SN and SESN populations. This intermediate distribution is consistent with predictions for blue Type IIb SN progenitors ($\sim 10^{4.5}$–$10^{5.5}\,L_{\odot}$) that evolve primarily via binary channels (N. Sravan et al. 2020).

We note that the inherent uncertainties in the luminosity estimation stem from two main assumptions. First, estimating the helium core mass relies on a canonical 1.4 $M_{\odot}$ compact remnant. Variations in the actual neutron star mass, alongside any minor contributions from the residual envelopes, may introduce an uncertainty of a few tenths of a solar mass to the pre-explosion mass budget. Second, the universal empirical relation Equation (5) carries intrinsic scatter associated with different stellar evolution pathways. As demonstrated by recent binary progenitor models (L. Dessart et al. 2024), varying binary interaction histories (e.g., different mass-transfer phases and envelope stripping efficiencies) can slightly alter the final core structure and surface luminosity, even for stars with identical initial masses. Consequently, the core mass–luminosity relation derived from such binary-stripped models can be systematically lower by approximately 0.04 dex compared to our adopted relation. However, owing to the logarithmic dependence in Equation (5), the combination of both the mass budget uncertainties and the intrinsic scatter in the relation translates to relatively small absolute shifts in the inferred luminosities. Therefore, these caveats do not alter our qualitative conclusions regarding the intermediate positions of our sample relative to the broader SN populations.

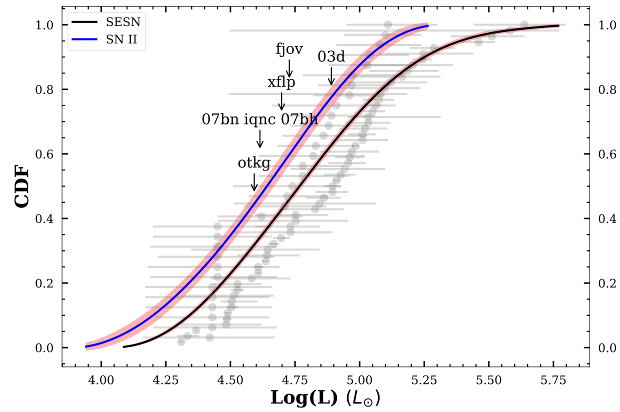

Figure 8. The CDFs of the inferred progenitor luminosities for the SESNe samples from D23, D24, and F. Taddia et al. (2018). The gray circles in the background represent the individual data points, and the red shaded region indicates the 1σ error bounds. The luminosity positions of all samples are marked by black arrows.

5. Conclusion

We present early multiwavelength photometric observations of seven SNe discovered by WFST, all of which show prominent shock-cooling emission at early times. The main conclusions of this work are summarized as follows:

1. All events show a clear double-peaked light-curve morphology. The early-excess emission is naturally interpreted as shock-cooling emission and typically persists for ∼3–5 days. This behavior closely resembles that observed in SESNe such as SN 2016gkg and SN 1993J, indicating partially stripped progenitors. The brightest event, WFST-PS240307bn, reaches an r-band primary peak absolute magnitude of −19.02, likely consistent with a Type Ic classification, while the remaining events peak at $M_r \sim -15.5$ to −17.3, comparable to typical Type IIb SNe.
2. By jointly modeling the shock-cooling and radioactive-powered phases using the P21 and Arnett frameworks, we derive physical constraints on the explosion and progenitor properties. The inferred ejecta masses ($\sim$1.1–2.6 $M_{\odot}$) place these events in the transitional regime between USSNe and normal SESNe. In addition, the modest envelope masses ($\sim$0.1–0.4 $M_{\odot}$), together with progenitor radii of $\sim$120–260 $R_{\odot}$ and luminosities of $10^{4.6}$–$10^{4.9}\,L_{\odot}$, imply extensive pre-explosion envelope stripping. Such substantial mass loss strongly favors a binary evolutionary origin.

Acknowledgments

This work was supported by the Strategic Priority Research Program of the Chinese Academy of Sciences (grant No. XDB0550300), the National Natural Science Foundation of China (NSFC; grant Nos. 12393811 and 12303047), the National Key Research and Development Program of China (grant Nos. 2023YFA1608100 and 2021YFA0718500), and the Natural Science Foundation of Hubei Province (grant No. 2023AFB321). J.J. acknowledges support from the Japan Society for the Promotion of Science (JSPS) KAKENHI (grant No. JP22K14069). K.M. acknowledges support from the Japan Society for the Promotion of Science (JSPS) KAKENHI grant (JP24KK0070, JP24H01810). The work is partly supported by the JSPS Open Partnership Bilateral Joint Research Projects between Japan and Finland (K.M. and H.K.; JPJSBP120229923). H.K. was funded by the Research Council of Finland projects 324504, 328898, and 353019. L.G. acknowledges financial support from CSIC, MCIN, and AEI 10.13039/501100011033 under projects PID2023-151307NB-I00, PIE 20215AT016, and CEX2020-001058-M.

The Wide Field Survey Telescope (WFST) is a joint facility of the University of Science and Technology of China and Purple Mountain Observatory.

Facility: WFST:2.5m.

Software: Astropy (The Astropy Collaboration et al. 2022), pandas (The pandas development team 2026), numpy (C. R. Harris et al. 2020), scipy (P. Virtanen et al. 2020), Jupyter-notebook (T. Kluyver et al. 2016), SWarp (E. Bertin 2010), SExtractor (E. Bertin & S. Arnouts 1996), superbol (M. Nicholl 2018), BAGPIPES (A. C. Carnall et al. 2018), astroquery (A. Ginsburg et al. 2019).

Appendix
Early-phase Blackbody SED Fitting Results

The fitting results of early-phase blackbody spectral energy distribution (SED) for the WFST sample are shown in Figure A1.

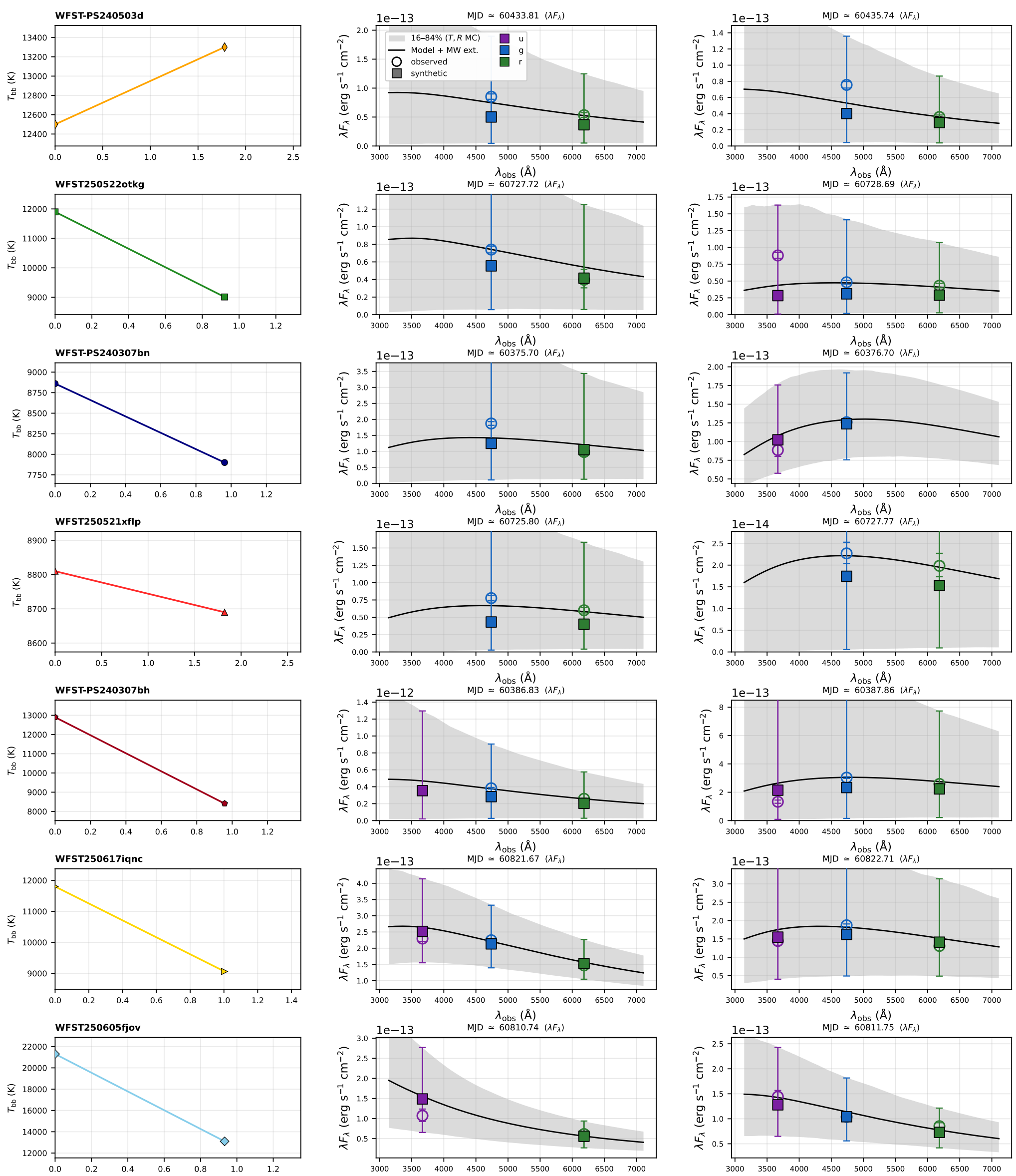

Figure A1. Early-phase blackbody SED fittings for the first two epochs of the WFST sample. Observed fluxes in u-/g-/r-bands are denoted by purple/blue/green circles with 1σ error, respectively. Black curves represent the best-fit Planck blackbody spectra, and SED-predicted fluxes integrated over the respective passband are denoted by squares.

ORCID iDs

Ji-an Jiang https://orcid.org/0000-0002-9092-0593
Qiliang Fang https://orcid.org/0000-0002-1161-9592
Liang-Duan Liu https://orcid.org/0000-0002-8708-0597
Qingfeng Zhu https://orcid.org/0000-0003-0694-8946
Yun-Wei Yu https://orcid.org/0000-0002-1067-1911
Keiichi Maeda https://orcid.org/0000-0003-2611-7269
Hanindyo Kuncarayakti https://orcid.org/0000-0002-1132-1366
Željko Ivezić https://orcid.org/0000-0001-5250-2633
Saurabh W. Jha https://orcid.org/0000-0001-8738-6011
Peter Yoachim https://orcid.org/0000-0003-2874-6464
Weiyu Wu https://orcid.org/0009-0003-9474-8457
Zhengyan Liu https://orcid.org/0000-0002-2242-1514
Andrew J. Connolly https://orcid.org/0000-0001-5576-8189
Wen Zhao https://orcid.org/0000-0002-1330-2329
Lulu Fan https://orcid.org/0000-0003-4200-4432

References

Arcavi, I., Hosseinzadeh, G., Brown, P. J., et al. 2017, ApJL, 837, L2
Armstrong, P., Tucker, B. E., Rest, A., et al. 2021, MNRAS, 507, 3125
Arnett, W. D. 1982, ApJ, 253, 785
Axelrod, T., Kantor, J., Lupton, R. H., & Pierfederici, F. 2010, SPIE, 7740, 437
Bersten, M. C., Folatelli, G., García, F., et al. 2018, Natur, 554, 497
Bertin, E. 2010, SWarp: Resampling and Co-adding FITS Images Together, Astrophysics Source Code Library, ascl:1010.068
Bertin, E., & Arnouts, S. 1996, A&AS, 117, 393
Blanton, M. R., Bershady, M. A., Abolfathi, B., et al. 2017, AJ, 154, 28
Bosch, J., Armstrong, R., Bickerton, S., et al. 2018, PASJ, 70, S5
Cardelli, J. A., Clayton, G. C., & Mathis, J. S. 1989, ApJ, 345, 245
Carnall, A. C., McLure, R. J., Dunlop, J. S., & Davé, R. 2018, MNRAS, 480, 4379
Carnall, A. C., McLure, R. J., Dunlop, J. S., et al. 2019, MNRAS, 490, 417
Chen, L., Wang, X., Wu, Q., et al. 2025, arXiv:2510.22997
Clocchiatti, A., & Wheeler, J. C. 1997, ApJ, 491, 375
DESI Collaboration, Abdul-Karim, M., Adame, A. G., et al. 2026, ApJ, 171, 285
Das, K. K., Kasliwal, M. M., Fremling, C., et al. 2023, ApJ, 959, 12
Das, K. K., Kasliwal, M. M., Sollerman, J., et al. 2024, ApJ, 972, 91
De, K., Kasliwal, M. M., Cantwell, T., et al. 2018, ApJ, 866, 72
Dessart, L., Gutiérrez, C. P., Ercolino, A., Jin, H., & Langer, N. 2024, A&A, 685, A169
Dessart, L., Hillier, D. J., Waldman, R., & Livne, E. 2013, MNRAS, 433, 1745
Dong, Y., Valenti, S., Ashall, C., et al. 2024, ApJ, 974, 316
Drout, M. R., Götberg, Y., Ludwig, B. A., et al. 2023, Sci, 382, 1287
Fang, Q., & Maeda, K. 2023, ApJ, 949, 93
Fang, Q., Maeda, K., Kuncarayakti, H., Sun, F., & Gal-Yam, A. 2019, NatAs, 3, 434
Fang, Q., Moriya, T. J., Maeda, K., Dorozsmai, A., & Silva-FarfÃąn, J. 2025a, ApJ, 990, 60
Fang, Q., Moriya, T. J., Maeda, K., et al. 2025b, ApJ, 986, 39
Feroz, F., Hobson, M. P., & Bridges, M. 2009, MNRAS, 398, 1601
Gal-Yam, A. 2017, Handbook of Supernovae (Springer), 195
Ginsburg, A., Sipőcz, B. M., Brasseur, C. E., et al. 2019, AJ, 157, 98
Harris, C. R., Millman, K. J., van der Walt, S. J., et al. 2020, Natur, 585, 357
Ivezić, Ž., Kahn, S. M., Tyson, J. A., et al. 2019, ApJ, 873, 111
Janka, H.-T. 2012, ARNPS, 62, 407
Jiang, J.-a., Doi, M., Maeda, K., & Shigeyama, T. 2018, ApJ, 865, 149
Jiang, J.-a., Doi, M., Maeda, K., et al. 2017, Natur, 550, 80
Jordi, K., Grebel, E. K., & Ammon, K. 2006, A&A, 460, 339
Karamehmetoglu, E., Taddia, F., Sollerman, J., et al. 2017, A&A, 602, A93
Kluyver, T., Ragan-Kelley, B., Pérez, F., et al. 2016, in Positioning and Power in Academic Publishing: Players, Agents and Agendas, ed. F. Loizides & B. Schmidt (IOS Press), 87
Liu, L.-D., Zhang, Y.-H., Yu, Y.-W., et al. 2025, ApJ, 992, 20
Lyman, J. D., Bersier, D., James, P. A., et al. 2016, MNRAS, 457, 328
Maeda, K., Jiang, J.-a., Shigeyama, T., & Doi, M. 2018, ApJ, 861, 78
Martinez, L., Bersten, M. C., Anderson, J. P., et al. 2022, A&A, 660, A40
Nicholl, M. 2018, RNAAS, 2, 230
Ouchi, R., & Maeda, K. 2017, ApJ, 840, 90
Pellegrino, C., Hiramatsu, D., Arcavi, I., et al. 2023, ApJ, 954, 35
Piro, A. L., Haynie, A., & Yao, Y. 2021, ApJ, 909, 209
Planck Collaboration, Aghanim, N., Akrami, Y., et al. 2018, A&A, 641, 67
Prentice, S. J., & Mazzali, P. A. 2017, MNRAS, 469, 2672
Reguitti, A., Pastorello, A., Smartt, S. J., et al. 2025, A&A, 698, A129
Rodríguez, Ó., Maoz, D., & Nakar, E. 2023, ApJ, 955, 71
Sapir, N., & Waxman, E. 2017, ApJ, 838, 130
Schlafly, E. F., & Finkbeiner, D. P. 2011, ApJ, 737, 103
Sravan, N., Marchant, P., Kalogera, V., Milisavljevic, D., & Margutti, R. 2020, ApJ, 903, 70
Stritzinger, M. D., Taddia, F., Burns, C. R., et al. 2018, A&A, 609, A135
Subrayan, B. M., Sand, D. J., Bostroem, K. A., et al. 2025, ApJL, 990, L68
Sukhbold, T., Ertl, T., Woosley, S. E., Brown, J. M., & Janka, H.-T. 2016, ApJ, 821, 38
Sukhbold, T., Woosley, S. E., & Heger, A. 2018, ApJ, 860, 93
Sun, N.-C., Maund, J. R., & Crowther, P. A. 2023, MNRAS, 521, 2860
Taddia, F., Stritzinger, M. D., Bersten, M., et al. 2018, A&A, 609, A136
Takahashi, K., Takiwaki, T., & Yoshida, T. 2023, ApJ, 945, 19
Temaj, D., Schneider, F. R. N., Laplace, E., Wei, D., & Podsiadlowski, P. 2024, A&A, 682, A123
The Astropy Collaboration, Price-Whelan, A. M., Lim, P. L., et al. 2022, ApJ, 935, 167
The pandas development team 2026, pandas-dev/pandas: Pandas (Version 2.2.3), Zenodo, doi:10.5281/zenodo.18328522
Virtanen, P., Gommers, R., Oliphant, T. E., et al. 2020, NatMe, 17, 261
Wang, Q., Armstrong, P., Zenati, Y., et al. 2023, ApJ, 943, L15
Wang, T., Liu, G., Cai, Z., et al. 2023, SCPMA, 66, 109512
Waxman, E., & Katz, B. 2017, in Handbook of Supernovae, ed. A. W. Alsabti & P. Murdin (Springer), 967
Woosley, S. E., Eastman, R. G., Weaver, T. A., & Pinto, P. A. 1994, ApJ, 429, 300
Yao, Y., De, K., Kasliwal, M. M., et al. 2020, ApJ, 900, 46
Yoon, S.-C., Dessart, L., & Clocchiatti, A. 2017, ApJ, 840, 10